A 2D BEM-FEM approach for time harmonic fluid-structure interaction analysis of thin elastic bodies[*]

J.D.R. Bordón, J.J. Aznárez, O. Maeso

Instituto Universitario de Sistemas Inteligentes y Aplicaciones Numéricas en Ingeniería,

Universidad de Las Palmas de Gran Canaria, Edificio Central del Parque Científico y Tecnológico del

Campus Universitario de Tafira, 35017 Las Palmas de Gran Canaria, Spain

`{jdrodriguez,jaznarez,omaeso}@iusiani.ulpgc.es`

Abstract

This paper deals with two-dimensional time harmonic fluid-structure interaction problems when the fluid is at rest, and the elastic bodies have small thicknesses. A BEM-FEM numerical approach is used, where the BEM is applied to the fluid, and the structural FEM is applied to the thin elastic bodies. From the fluid point of view, the thin elastic bodies are considered of null thickness. This assumption is treated using simultaneously the Singular Boundary Integral Equation and the Hypersingular Boundary Integral Equation. It is assumed that the thin elastic bodies are under the Euler-Bernoulli hypotheses with added rotational inertia. The BEM equations (fluid) and the FEM equations (thin bodies) are coupled using appropriate equilibrium and compatibility conditions. The developed BEM-FEM model requires a simple discretization and leads to a small number of degrees of freedom, although it has some limitations that are studied in some depth. This approach is validated with existing results in the field of sound barriers, and new results using complex barrier shapes are presented. Also, a parametric study about a straight wall immersed in a fluid is done, which provides results of practical usage.

Keywords: SBIE/HBIE dual boundary formulation, BEM-FEM coupling, thin bodies, fluid-structure interaction, wave propagation, flexible sound barriers

1 Introduction

The Boundary Element Method (BEM) and the Finite Element Method (FEM) can handle problems such as heat conduction, electrostatics, elastostatics and elastodynamics, just to name a few. Nevertheless, each method has its own strengths and weaknesses [4]. The combination of both methods comes up when neither the FEM nor the BEM is adequate to face a problem. This is the case of the Fluid-Structure Interaction (FSI) problem posed here, in which there are thin elastic bodies surrounded by a fluid where wave propagation phenomena take place.

The BEM is widely used for time harmonic wave propagation in fluids, viscoelastic solids, poroelastic solids, and when regions of any of these types are interacting with each other. When each region is treated by the BEM, the approach is called BEM-BEM. A lot of work has been done about it when applied to dynamic Fluid-Soil-Structure Interaction (FSSI) and its particular cases: FSI and Soil-Structure Interaction (SSI). In this field, the work of Domínguez and co-workers [41, 16, 3] must be highlighted. There are very complete reviews [5, 6, 21]. Also, the BEM-BEM approach for FSI problems in the field of sound barriers has been studied [50]. Taking this into account, the problem posed here can be solved by the BEM-BEM approach. However, when thin elastic solids appear in a problem, some interrelated difficulties emerge in the BEM-BEM approach: discretization needs, quasi-singular integration accuracy, and the Linear System of Equations (LSE) degeneracy.

A thin body is characterized by having faces very close each other. Depending on the element size, the relative distance between an element and any node not belonging to it can be very small. This relative distance is the most relevant factor when evaluating BEM quasi-singular integrals. Thus, the maximum size of the elements heavily depends on the quasi-singular integration capabilities. Several quasi-singular integration strategies have been developed through the years. It is worth mentioning two simple but powerful classical strategies: adaptive subdivision with selection of the quadrature order [32, 26] and adaptive cubic transformation [52, 53]; a mix of both is used in this work. When body thickness is too small, more elaborated strategies are needed. Among others, Liu and co-workers worked on it in 2D [36] and in 3D [35, 34, 12], and they showed that very thin bodies can be efficiently treated. Recent works contain brief updated reviews of quasi-singular integration strategies [55, 57, 56].

Given an exterior region with a thin body inside it, Krishnasamy et al. [27] showed that if only Singular Boundary Integral Equations (SBIE) are applied to build the BEM final LSE, then its condition number get worse as thickness decreases, becoming completely degenerated if the thickness is null. If the thin body is not surrounded by an exterior region, i.e. the thin body is considered alone, Liu et al. [34] demonstrated that, if the primary variables are not constrained at all boundaries, then the LSE does not degenerate. In both cases, the discretization must be carefully done, and a capable quasi-singular strategy is mandatory.

If the thin body region is a viscoelastic region, the well known structural beam/shell hypotheses are applicable to

---

model it. Doing so, its dimensional space is reduced to 1D for a beam, and to 2D for a shell. The FEM is appropriate to discretize these structural elements, which reduces heavily the discretization effort and the number of degrees of freedom when compared to the BEM. However, from the point of view of the region that contains the thin body, the FEM discretization is seen as a degenerated geometry, i.e. a null thickness geometry, that can not be directly handled by the conventional BEM. Two ways of solving this difficulty for our problem are: the multiregion approach [7], or employing the Hypersingular BIE (HBIE) in combination with the SBIE [27]. The multiregion approach needs the definition of some artificial boundaries, which can be hard to do. However, the SBIE/HBIE dual boundary formulation is applied directly to the null thickness geometry.

The SBIE/HBIE dual boundary formulation emerged to solve fracture mechanics problems [15, 47], but it has been applied to other problems like sound propagation [30, 31, 48, 49]. Its main drawback is handling with the HBIE, which is more difficult to treat than the SBIE. The HBIE has received much attention, particularly about the continuity requirements [29, 39, 40] and regularization techniques [28, 20, 51, 10]. The Cauchy Principal Value (CPV) and Hadamard Finite Part (HFP) definitions are often used to deal with it, see for example [23]. Nevertheless, in line with Guiggiani [20], we prefer making explicit the whole limiting process in order to see clearly how the unbounded terms cancel out, and only regular or weakly singular integrals remain. We propose coupling directly the SBIE/HBIE dual boundary formulation with the structural FEM.

The idea of BEM-FEM coupling arose since the BEM beginnings [4]. It is used to overcome difficulties such as non-linearities, or to reduce the discretization and computational effort, that is our case. An example of its usefulness could be seen in the work of Padrón et al. [42, 43, 44], who coupled FEM beams (piles) with 3D BEM viscoelastic regions (stratified soils). Most works about BEM-FEM applied to FSI deal with closed thin structures like boxes, cylinders, spheres, ships or submarines [8, 54], where a dual boundary formulation is not needed. A much smaller number of works deal with open thin structures, and their methodologies differ from ours. Jean [25] used a variational approach discretized with 2D boundary elements for the fluid and 2D finite elements for the structure. Z.S. Chen et al. [13] used a Symmetric Galerkin BEM for 3D FSI problems. Recently, L.L. Chen et al. [11] used the FEM in combination with the Wideband Fast Multipole Method to handle 2D FSI problems.

The proposed direct BEM-FEM approach is presented as follows. The fluid is treated by the BEM. From the fluid region point of view, the structure is considered as a null thickness body, and the simultaneous application of the SBIE and the HBIE is used to handle it. The fluid basic formulation is shown at 2.1, and some details of the HBIE regularization process are given at A. The thin bodies are discretized using structural straight FEM elements with Euler-Bernoulli hypotheses with added rotational inertia, which is shown at 2.2. At 2.3, the BEM equations (fluid) and the FEM equations (thin bodies) are coupled using equilibrium and compatibility conditions. Two limitations exist in this approach: the null thickness assumption of the thin elastic body from the fluid point of view, and the Euler-Bernoulli hypotheses of the thin elastic body; they

are studied at 2.4. The proposed BEM-FEM approach is validated at 3.1. In order to demonstrate its potential, complex sound barrier shapes are studied at 3.2, and a parametric study about a straight wall is done at 3.3.

2 Methodology

The problem consists in the harmonic analysis of a two-dimensional domain composed by a fluid region and many viscoelastic thin regions (thin bodies). Onwards, as usual in the harmonic analysis, the frequency is denoted as f, and the angular frequency is $\omega = 2\pi f$.

2.1 Fluid (BEM)

The fluid is considered homogeneous, inviscid, at rest, its body forces are neglected, and the excitations are low enough to admit small disturbances (linear behaviour). As it is well known, under these hypotheses the governing equation is the Helmholtz PDE.

Let $\Omega \subset \mathbb{R}^2$ be a fluid region, $\tilde{\rho}$ its density, and $\tilde{c}$ its wave propagation speed, the pressure p at any point $\mathbf{x} \in \Omega$ obeys:

$$\nabla^2 p + k^2 p = 0 \quad \text{in} \quad \Omega \tag{1}$$

where k is the wave number ($k = \omega/\tilde{c}$), and sources are neglected for the sake of brevity. The boundary of the region Ω is denoted as $\Gamma = \partial\Omega$, and the normal vector $\mathbf{n}$ is defined outwards. The pressure p acts as the primary variable, while the secondary variable could be the pressure flux q or the displacement in the normal direction u_n:

$$q = \frac{\partial p}{\partial n}, \quad u_n = \frac{1}{\tilde{\rho}\omega^2}\frac{\partial p}{\partial n} \tag{2}$$

The latter is physically more meaningful than the former, and is used when establishing compatibility conditions. However, q is chosen as the secondary variable, which is more common in the literature.

2.1.1 Singular BIE

The pressure BIE of (1) applied at a point $\mathbf{x}_i$ (collocation point) is:

$$c p_i + \int_\Gamma q^* p \, d\Gamma = \int_\Gamma p^* q \, d\Gamma \tag{3}$$

where each term of the equation is:

$$\begin{aligned} c &= \begin{cases} 0, \ \mathbf{x}_i \notin \Omega \cup \Gamma \\ 1, \ \mathbf{x}_i \in \Omega \\ ]0,1[, \ \mathbf{x}_i \in \Gamma \end{cases} \\ p^* &= \frac{1}{2\pi}\mathrm{K}_0\left(ikr\right) \\ q^* &= -\frac{ik}{2\pi}\mathrm{K}_1\left(ikr\right)\frac{\partial r}{\partial n} \end{aligned} \tag{4}$$

where i is the imaginary unit, $r = \left|\mathbf{x} - \mathbf{x}_i\right|$ is the distance between observation and collocation points, and $\mathrm{K}_n\left(z\right)$ is the

modified Bessel function of the second kind, order n, and argument z. $\mathrm{K}_n(z)$ properties and expansions can be found in [1, Chapter 9].

When $\mathbf{x}_i$ is taken to Γ, the integrals in (3) contain a singularity, but they are integrable if a limiting process from inside or outside Ω is followed. The integration domain Γ is partitioned as $\Gamma = \lim_{\epsilon \to 0}\{(\Gamma - e_i^\epsilon) + \Gamma_i^\epsilon\}$, where e_i^ϵ is the exclusion zone of Γ, and Γ_i^ϵ is an arc of radius ϵ that surrounds $\mathbf{x}_i$. The integration over Γ_i^ϵ produces the free-term c, which is in the interval $]0,1[$, being $1/2$ if Γ is smooth at the collocation point, i.e. $\Gamma(\mathbf{x}_i) \in \mathscr{C}^1$. The integrals over $\Gamma - e_i^\epsilon$ are at most weakly singular, as is well known. In this work, the collocation points are placed at smooth boundary points, so, in the following, the equations are written under this hypothesis.

If the boundary Γ is partitioned in N_e elements, $\Gamma = \cup_1^{N_e} \Upsilon_j$, and geometry, p, and q are interpolated over each element Υ_j using Lagrange elements, then the discretized SBIE can be written as:

$$\frac{1}{2}\boldsymbol{\phi}_i^{\bar{j}} \cdot \mathbf{p}^{\bar{j}} + \sum_{j=1}^{j=N_e} \mathbf{h}_i^j \cdot \mathbf{p}^j = \sum_{j=1}^{j=N_e} \mathbf{g}_i^j \cdot \mathbf{q}^j, \quad \mathbf{x}_i \begin{cases} \in \Upsilon_{\bar{j}} \\ \notin \partial \Upsilon_{\bar{j}} \end{cases} \quad (5)$$

where $\mathbf{h}_i^j$ and $\mathbf{g}_i^j$ are the integral kernels of the element j when the SBIE is applied at $\mathbf{x}_i$. The element $\bar{j}$ is the one that contains $\mathbf{x}_i$, and $\boldsymbol{\phi}_i^{\bar{j}}$ is the vector of shape functions of the element $\bar{j}$ evaluated at $\mathbf{x}_i$.

2.1.2 Hypersingular BIE

In order to obtain the pressure flux BIE, the derivative of the pressure BIE with respect to a direction $\mathbf{d}$ is taken:

$$c\left(\frac{\partial p}{\partial d}\right)_i + \int_\Gamma \frac{\partial q^*}{\partial d} p \, d\Gamma = \int_\Gamma \frac{\partial p^*}{\partial d} q \, d\Gamma, \quad \mathbf{x}_i \notin \Gamma \quad (6)$$

where each term of the equation is:

$$c = \begin{cases} 0, & \mathbf{x}_i \notin \Omega \cup \Gamma \\ 1, & \mathbf{x}_i \in \Omega \end{cases}$$

$$\frac{\partial p^*}{\partial d} = -\frac{ik}{2\pi} \mathrm{K}_1(ikr) \frac{\partial r}{\partial d} \quad (7)$$

$$\frac{\partial q^*}{\partial d} = \frac{ik}{2\pi}\left[ik\mathrm{K}_2(ikr)\frac{\partial r}{\partial d}\frac{\partial r}{\partial n} + \frac{1}{r}\mathrm{K}_1(ikr)(\mathbf{d} \cdot \mathbf{n})\right]$$

When $\mathbf{x}_i$ is taken to Γ, $\mathbf{d} = \mathbf{n}_i$ is used, where $\mathbf{n}_i$ is the normal vector at the collocation point. The left-hand side integral of (6) contains a singularity, which is stronger than the right-hand side integral of (6) and the integrals of (3). Thus, when $\mathbf{x}_i$ is taken to Γ, the pressure flux BIE is called the Hypersingular BIE. Given a hypersingular integral $I = \int_A^B F(x)/(x - x_i)^2 \, dx$, $A < x_i < B$, if F has certain continuity properties, then I exists. F must belong to the Hölder function space $\mathscr{C}^{1,\alpha}$ [40]. To do so, the pressure must be differentiable at the collocation point, i.e. $p(\mathbf{x}_i) \in \mathscr{C}^1$.

Similarly to the SBIE, a limiting process where $\Gamma = \lim_{\epsilon \to 0}\{(\Gamma - e_i^\epsilon) + \Gamma_i^\epsilon\}$ is needed. The integration over Γ_i^ϵ not only produces a free-term, but also produces an unbounded term:

$$\frac{1}{2}\left(\frac{\partial p}{\partial n_i}\right)_i - \frac{p_i}{\pi}\lim_{\epsilon \to 0}\left(\frac{1}{\epsilon}\right) + \lim_{\epsilon \to 0}\int_{\Gamma - e_i^\epsilon}\frac{\partial q^*}{\partial n_i} p \, d\Gamma = \lim_{\epsilon \to 0}\int_{\Gamma - e_i^\epsilon}\frac{\partial p^*}{\partial n_i} q \, d\Gamma$$
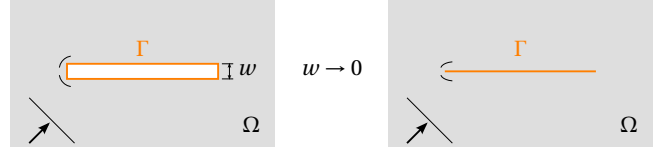

Figure 1: Approximation when using the null thickness assumption

$$(8)$$

In the following, the right-hand and the left-hand side integrals of (8) are called L and M, respectively. L is regular since has the same kind of singularity as the left-hand side integral of (3). Taking into account that $\mathrm{K}_1(ikr) = 1/(ikr) + \mathrm{K}_1^R(ikr)$, where $\mathrm{K}_1^R(ikr) = \mathcal{O}(r \ln r)$, M can be decomposed into:

$$M = \frac{(ik)^2}{2\pi}\lim_{\epsilon \to 0}\int_{\Gamma - e_i^\epsilon}\mathrm{K}_2(ikr)\frac{\partial r}{\partial n_i}\frac{\partial r}{\partial n} p \, d\Gamma +$$

$$+ \frac{1}{2\pi}\lim_{\epsilon \to 0}\int_{\Gamma - e_i^\epsilon}\frac{1}{r^2}(\mathbf{n}_i \cdot \mathbf{n}) p \, d\Gamma \quad (9)$$

$$+ \frac{ik}{2\pi}\lim_{\epsilon \to 0}\int_{\Gamma - e_i^\epsilon}\frac{1}{r}\mathrm{K}_1^R(ikr)(\mathbf{n}_i \cdot \mathbf{n}) p \, d\Gamma = M_1 + M_2 + M_3$$

where M_1 is regular, M_2 is hypersingular and M_3 is weakly singular. A regularization process is required for M_2 (see A). It is based on Sáez et al. contributions [45], who applied it to elastostatics. Unlike Sáez et al., M_2 is regularized before discretization, which gives some interesting insights into this integral. Through the regularization process of M_2 emerges an unbounded term that cancels out the one that appears in (8), which leads to the regularized HBIE. As did with the SBIE, the discretized HBIE can be written as:

$$\sum_{j=1}^{j=N_e} \mathbf{m}_i^j \cdot \mathbf{p}^j = -\frac{1}{2}\boldsymbol{\phi}_i^{\bar{j}} \cdot \mathbf{q}^{\bar{j}} + \sum_{j=1}^{j=N_e} \mathbf{l}_i^j \cdot \mathbf{q}^j, \quad \mathbf{x}_i \begin{cases} \in \Upsilon_{\bar{j}} \\ \notin \partial \Upsilon_{\bar{j}} \end{cases} \quad (10)$$

where $\mathbf{m}_i^j$ and $\mathbf{l}_i^j$ are the integral kernels of the element j when the HBIE is applied at $\mathbf{x}_i$ with a normal $\mathbf{n}_i$. Only the integral kernel vector $\mathbf{m}_i^{\bar{j}}$ of the element $\bar{j}$ uses the regularized M.

2.1.3 BIEs for coincident boundaries

When nearly coincident boundaries (nearly coplanar boundaries) belong to the same region (i.e. a crack, a thin void, a thin inclusion, or a thin scatterer) the LSE is nearly-singular. In the limit when boundaries are coincident (null thickness discontinuity), the LSE becomes singular. The simultaneous application of the SBIE and the HBIE can solve this difficulty [27]. The null thickness assumption is very interesting because it can greatly reduce the discretization and the computational effort at the expense of an approximation of the field around the discontinuity (see Figure 1). The computational cost reduction can be > 60% [30, Table 1], depending on the problem, the analysed frequencies, and the implementation.

Let Γ be the boundary of a region Ω, resulting from the approaching of two identical boundaries, whose normals are pointing at each other, until they are coincident. One of the boundaries is chosen as the positive face Γ^+ of Γ, which is used as the reference face for the whole Γ. Thus the normal vectors $\mathbf{n}$ and $\mathbf{n}_i$ are defined on it. Each face has two variables, the pressure and the pressure flux, so there are four variables at the collocation point i: p_i^+, q_i^+, p_i^- and q_i^-. The limiting process can be done using the integration domain depicted in Figure 2:

$$\Gamma = \lim_{\epsilon \to 0} \left\{ \left[\Gamma^+ - \left(e_i^\epsilon \right)^+ \right] + \left(\Gamma_i^\epsilon \right)^+ + \left[\Gamma^- - \left(e_i^\epsilon \right)^- \right] + \left(\Gamma_i^\epsilon \right)^- \right\} \quad (11)$$

The singularity is avoided twice: when integrating over Γ^+, and when integrating over Γ^-. The resulting SBIE is:

$$\frac{1}{2} p_i^+ + \lim_{\epsilon \to 0} \int\limits_{\Gamma^+ - \left(e_i^\epsilon \right)^+} q^* p \, \mathrm{d}\Gamma_i + \frac{1}{2} p_i^- + \lim_{\epsilon \to 0} \int\limits_{\Gamma^- - \left(e_i^\epsilon \right)^-} q^* p \, \mathrm{d}\Gamma_i =$$

$$= \lim_{\epsilon \to 0} \int\limits_{\Gamma^+ - \left(e_i^\epsilon \right)^+} p^* q \, \mathrm{d}\Gamma + \lim_{\epsilon \to 0} \int\limits_{\Gamma^- - \left(e_i^\epsilon \right)^-} p^* q \, \mathrm{d}\Gamma, \quad \mathbf{x}_i \in \Gamma$$

$$(12)$$

and the resulting HBIE is:

$$\frac{1}{2} q_i^+ - \frac{p_i^+}{\pi} \lim_{\epsilon \to 0} \left(\frac{1}{\epsilon} \right) + \lim_{\epsilon \to 0} \int\limits_{\Gamma^+ - \left(e_i^\epsilon \right)^+} \frac{\partial q^*}{\partial n_i} p \, \mathrm{d}\Gamma -$$

$$- \frac{1}{2} q_i^- - \frac{p_i^-}{\pi} \lim_{\epsilon \to 0} \left(\frac{1}{\epsilon} \right) + \lim_{\epsilon \to 0} \int\limits_{\Gamma^- - \left(e_i^\epsilon \right)^-} \frac{\partial q^*}{\partial n_i} p \, \mathrm{d}\Gamma =$$

$$= \lim_{\epsilon \to 0} \int\limits_{\Gamma^+ - \left(e_i^\epsilon \right)^+} \frac{\partial p^*}{\partial n_i} q \, \mathrm{d}\Gamma + \lim_{\epsilon \to 0} \int\limits_{\Gamma^- - \left(e_i^\epsilon \right)^-} \frac{\partial p^*}{\partial n_i} q \, \mathrm{d}\Gamma, \quad \mathbf{x}_i \in \Gamma$$

$$(13)$$

where $q_i^+ = (\partial p^+ / \partial n_i)_i$ and $q_i^- = -(\partial p^- / \partial n_i)_i$. Similarly to 2.1.2, two unbounded terms have been produced when solving the integrals over $(\Gamma_i^\epsilon)^+$ and $(\Gamma_i^\epsilon)^-$. Likewise, the regularization process of the left hand side integrals of (13) produces two unbounded terms that cancel out the previous ones.

The discretization process is similar to that followed for the SBIE and the HBIE, with the condition that the faces Γ^+ and Γ^- have the same discretization. Because of that, it is possible to build a new type of element Υ_j that is composed by two sub-elements Υ_j^+ and Υ_j^-. The variables of Υ_j can be written as:

$$\mathbf{p}^j = \left\{ \ \left(\mathbf{p}^j \right)^+ \quad \left(\mathbf{p}^j \right)^- \ \right\}, \quad \mathbf{q}^j = \left\{ \ \left(\mathbf{q}^j \right)^+ \quad \left(\mathbf{q}^j \right)^- \ \right\} \quad (14)$$

Taking advantage of $\mathbf{n} = \mathbf{n}^+ = -\mathbf{n}^-$, the integral kernels of Υ_j can be written only in terms of the integral kernels of the sub-element Υ_j^+. The discretized SBIE and the discretized HBIE for a collocation point $\mathbf{x}_i$ belonging to coincident boundaries are:

$$\frac{1}{2} \left\{ \ \boldsymbol{\phi}_i^{\bar{\jmath}} \quad \boldsymbol{\phi}_i^{\bar{\jmath}} \ \right\} \cdot \mathbf{p}^j + \sum_{j=1}^{j=N_e} \mathbf{h}_i^j \cdot \mathbf{p}^j = \sum_{j=1}^{j=N_e} \mathbf{g}_i^j \cdot \mathbf{q}^j \quad (15)$$
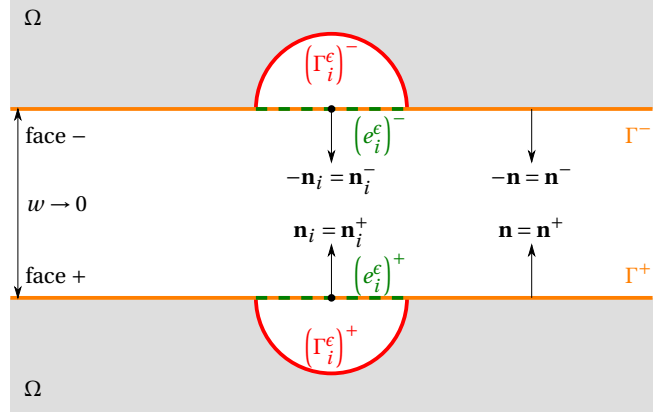

Figure 2: Singularity treatment for coincident boundaries

$$\sum_{j=1}^{j=N_e} \mathbf{m}_i^j \cdot \mathbf{p}^j = \frac{1}{2} \left\{ \ -\boldsymbol{\phi}_i^{\bar{\jmath}} \quad \boldsymbol{\phi}_i^{\bar{\jmath}} \ \right\} \cdot \mathbf{q}^{\bar{\jmath}} + \sum_{j=1}^{j=N_e} \mathbf{l}_i^j \cdot \mathbf{q}^j \quad (16)$$

If the fluid is uncoupled, then these equations are handled in the usual way, but having Γ^+ and Γ^- independent boundary conditions. If the fluid is coupled with a thin elastic body, which is the main input of this paper, these equations together with those presented in 2.2 and 2.3 are used.

2.1.4 Discretization and collocation procedure

The discretized equations written above have been developed under $\Gamma(\mathbf{x}_i) \in \mathscr{C}^1$ and $p(\mathbf{x}_i) \in \mathscr{C}^1$ hypotheses at the collocation point. By doing so, the collocation procedure described here can be applied simultaneously to the HBIE and the SBIE at coincident boundaries, giving a uniform approach to build the BEM equations.

The $\mathscr{C}^1$ requirement can be fulfilled by many ways, among others: cubic splines [33], an interpolation algorithm [19], Overhauser elements [9] or discontinuous Lagrange elements [45]. The way we deal with it is using continuous isoparametric Lagrange elements with non-nodal collocation at vertex nodes, and adding up the BIEs associated with each vertex node. This strategy is known as the Multiple Collocation Approach (MCA), and it was introduced by Gallego et al. [18, 17, 2]. It is very simple, gives accurate results, and makes BEM-FEM coupling relatively easy. In this work, quadratic elements are used.

Given a vertex node i and its elements Υ_1 and Υ_2, two SBIEs are added up to build the equation associated with the node: one SBIE is collocated inside the element 1 at $\mathbf{x}_{i'}^1$, and the other SBIE is collocated inside the element 2 at $\mathbf{x}_{i'}^2$; the same is done with HBIEs (see Figure 3). Let δ be defined as the displacement of the collocation point towards the inside of the element. Given an element with a local system of coordinates $-1 \leq \xi \leq 1$, if ξ_i is the nodal position of the node i, then the local coordinate $\xi_{i'}$ of the displaced collocation point is:

$$\xi_{i'} = \xi_i (1 - \delta), 0 < \delta < 1 \Rightarrow \mathbf{x}_{i'} = \mathbf{x}(\xi_{i'}) \quad (17)$$

4

Figure 3: Multiple Collocation Approach

Figure 4: Three nodes / eight degrees of freedom FEM beam element
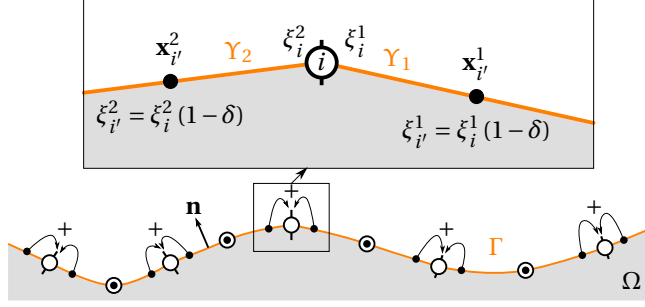
Note that $\delta = 0$ gives a collocation point at the nodal position, while $\delta = 1$ gives a collocation point at the element centre.

A question that arises is how much the collocation point should be displaced from the nodal position. Ariza et al. [2] used a value of $\delta = 0.25$, although it was not explained why. To the authors' knowledge, there is no published work about an optimum value of δ for the MCA. Nevertheless, the MCA can be related to discontinuous elements because the set-up of the collocation points is the same. Marburg [38] studied the optimum position of nodes of discontinuous elements for a sound propagation problem. He found that nodes located at the zeros of the Legendre polynomials gives optimum results. He also stated that the hypersingular formulation may have other optimal locations. Thus, we use $\delta = 0.2254$.

2.2 Thin elastic bodies (FEM)

In a plane deformation problem, a thin body has infinite width along x_3, and finite thickness w and length L in the $x_1 - x_2$ plane. Under these conditions, the thin body could be considered as a beam with a cross section $A = w \cdot 1$, a length L, and a modified Young's modulus $E = E_m/(1 - v^2)$, where E_m is the Young's modulus of the material and v its Poisson's ratio. Onwards, when the term "beam" is used, it must be understood this way.

Let Ω_s be a thin elastic body. It can be split into straight beam FEM elements Υ_j, which are under the Euler-Bernoulli hypotheses with added rotational inertia. In order to have a node-to-node correspondence with a quadratic BEM element, a beam FEM element with three nodes and eight degrees of freedom is considered [42] (see Figure 4). The vertex nodes $i = 1, 2$ have translation $u_1^{(i)}, u_2^{(i)}$ and rotation $\theta^{(i)}$, while the central node $i = 3$ has only translation $u_1^{(3)}, u_2^{(3)}$. Each element has a density ρ, a modified elastic modulus E, a thickness w, an inertia $I = (1/12) \cdot w^3 \cdot 1$, and a length L. Damping of hysteretic type is introduced by defining a complex Young's modulus $E = \text{Re}(E)(1 + i2\xi)$, where ξ is the damping coefficient.

Because axial behaviour and lateral behaviour are decoupled, axial and lateral elemental matrices can be obtained separately in the local system of coordinates. From now on, variables carrying an apostrophe are variables expressed in the local system of coordinates.

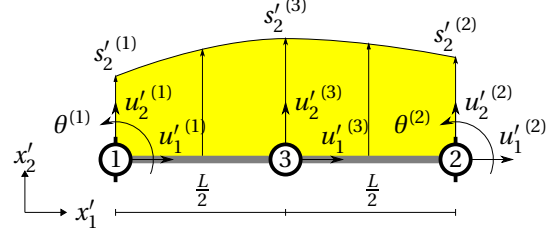The axial displacement u_1' is interpolated using a Lagrange quadratic element:

$$u_1'(\xi) = \left\{ \begin{array}{ccc} \phi_1 & \phi_2 & \phi_3 \end{array} \right\} \cdot \left\{ \begin{array}{ccc} u_1'^{(1)} & u_1'^{(2)} & u_1'^{(3)} \end{array} \right\}^T = \boldsymbol{\phi}^T \cdot \mathbf{u}'^a \tag{18}$$

The axial stiffness matrix and the axial translation mass matrix are obtained by using the Principle of Virtual Displacements, respectively:

$$K_{ij}'^{\,a} = \frac{2}{L} E A \int_{-1}^{1} \frac{d\phi_i}{d\xi} \frac{d\phi_j}{d\xi} \, d\xi$$
$$M_{ij}'^{\,ta} = \frac{L}{2} \rho A \int_{-1}^{1} \phi_i \phi_j \, d\xi \tag{19}$$

The lateral displacement u_2' is taken as a fourth degree polynomial in $-1 \le \xi \le 1$. The lateral displacement and the rotation are:

$$u_2'(\xi) = \boldsymbol{\varphi}^T \cdot \mathbf{u}'^l, \quad \theta(\xi) = \boldsymbol{\vartheta}^T \cdot \mathbf{u}'^l \tag{20}$$

where:

$$\mathbf{u}'^l = \left\{ \begin{array}{ccccc} u_2'^{(1)} & \theta^{(1)} & u_2'^{(2)} & \theta^{(2)} & u_2'^{(3)} \end{array} \right\}^T \tag{21}$$

$$\boldsymbol{\varphi} = \left\{ \begin{array}{c} \varphi_1 \\ \varphi_2 \\ \varphi_3 \\ \varphi_4 \\ \varphi_5 \end{array} \right\} = \left\{ \begin{array}{c} \frac{1}{4}\xi(-3 + 4\xi + \xi^2 - 2\xi^3) \\ \frac{L}{8}\xi(-1 + \xi + \xi^2 - \xi^3) \\ \frac{1}{4}\xi(3 + 4\xi - \xi^2 - 2\xi^3) \\ \frac{L}{8}\xi(-1 - \xi + \xi^2 + \xi^3) \\ 1 - 2\xi^2 + \xi^4 \end{array} \right\}, \quad \boldsymbol{\vartheta} = \frac{2}{L}\frac{d\boldsymbol{\varphi}}{d\xi} \tag{22}$$

The lateral stiffness matrix, the lateral translation mass matrix and the lateral rotation mass matrix are obtained by using the Principle of Virtual Displacements, respectively:

$$K_{ij}'^{\,l} = \left(\frac{2}{L}\right)^3 E I \int_{-1}^{1} \frac{d^2\varphi_i}{d\xi^2} \frac{d^2\varphi_j}{d\xi^2} \, d\xi$$
$$M_{ij}'^{\,tl} = \frac{L}{2} \rho A \int_{-1}^{1} \varphi_i \varphi_j \, d\xi$$
$$M_{ij}'^{\,r} = \frac{L}{2} \rho I \int_{-1}^{1} \vartheta_i \vartheta_j \, d\xi \tag{23}$$

The lateral distributed load s_2' along the beam is interpolated using a Lagrange quadratic element:

$$s_2'(\xi) = \left\{ \begin{array}{ccc} \phi_1 & \phi_2 & \phi_3 \end{array} \right\} \cdot \left\{ \begin{array}{ccc} s_2'^{(1)} & s_2'^{(2)} & s_2'^{(3)} \end{array} \right\}^T = \boldsymbol{\phi}^T \cdot \mathbf{s}_2'$$

The load s_2' can be transformed into equivalent nodal forces and moments by using the Principle of Virtual Work:

$$S'^{l}_{ij} = \frac{L}{2}\int_{-1}^{1} \vartheta_i \phi_j \, \mathrm{d}\xi, \quad i = 1,\dots,5, \; j = 1,\dots,3 \qquad (25)$$

The axial and lateral kinematic variables can be gathered together in $\mathbf{u}'$, and the lateral distributed load vector can be re-ordered as $\mathbf{s}'$:

$$\mathbf{u}' = \left\{ \; u_1'^{(1)} \quad u_2'^{(1)} \quad \theta^{(1)} \quad u_1'^{(2)} \quad u_2'^{(2)} \quad \theta^{(2)} \quad u_1'^{(3)} \quad u_2'^{(3)} \; \right\}^T$$

$$\mathbf{s}' = \left\{ \; \varnothing \quad s_2'^{(1)} \quad \varnothing \quad \varnothing \quad s_2'^{(2)} \quad \varnothing \quad \varnothing \quad s_2'^{(3)} \; \right\}^T$$

$$(26)$$

so that a stiffness matrix $\mathbf{K}'$ is obtained by combining $\mathbf{K}'^a$ and $\mathbf{K}'^l$, a mass matrix $\mathbf{M}'$ is obtained by combining $\mathbf{M}'^{ta}$ and $\mathbf{M}'^{tl} + \mathbf{M}'^r$, and a distributed load matrix $\mathbf{S}'$ is obtained by re-ordering the matrix $\mathbf{S}'^l$. In the harmonic regime, the dynamic equilibrium equation in global coordinates for a given element is:

$$\left[\mathbf{L} \cdot \left[\mathbf{K}' - \omega^2 \mathbf{M}' \right] \cdot \mathbf{L}^T \right] \cdot \mathbf{u} = \left[\mathbf{L} \cdot \mathbf{S}' \right] \cdot \mathbf{s}'$$

$$\mathbf{K}_h \cdot \mathbf{u} = \mathbf{Q} \cdot \mathbf{s}' \qquad (27)$$

where $\mathbf{L}$ is the coordinate transformation matrix of the element. This FEM equation is assembled considering all vertex nodes as rigid joints. It must be noticed that $\mathbf{s}'$ (distributed lateral loads) is unknown when coupled with the fluid. The element matrices can be easily obtained from (19), (23) and (25), or seen in [42] (except $\mathbf{M}'^r$).

2.3 Fluid-structure coupling (BEM-FEM)

Once the fluid equations (BEM) and the thin elastic bodies equations (FEM) have been posed, it is possible to combine both by using coupling equations. Let Υ_j be a BEM-FEM fluid-structure element composed by three sub-elements: Υ_j^+, Υ_j^- and Υ_j^s; being Υ_j^+ and Υ_j^- the sub-elements associated with both faces of the coincident boundaries of the fluid, and Υ_j^s the sub-element associated with the thin elastic body (see Figure 5). Since the fluid is inviscid, it interacts only laterally with the thin elastic body. Therefore, only lateral compatibility and equilibrium have to be established. The normal displacements of the fluid at the boundary (2) must coincide with the beam lateral displacements u_2', for a given node i:

$$u_2'^{(i)} = -\frac{1}{\tilde{\rho}\omega^2}q_i^+, \quad u_2'^{(i)} = \frac{1}{\tilde{\rho}\omega^2}q_i^- \qquad (28)$$

that leads to $q_i^+ = -q_i^-$. In (27), the displacements are expressed in the global system of coordinates, so their projection onto the x_2' axis gives the lateral displacements:

$$\mathbf{u}^{(i)} \cdot \mathbf{x}_2' = -\frac{1}{\tilde{\rho}\omega^2}q_i^+, \quad \mathbf{u}^{(i)} \cdot \mathbf{x}_2' = \frac{1}{\tilde{\rho}\omega^2}q_i^- \qquad (29)$$
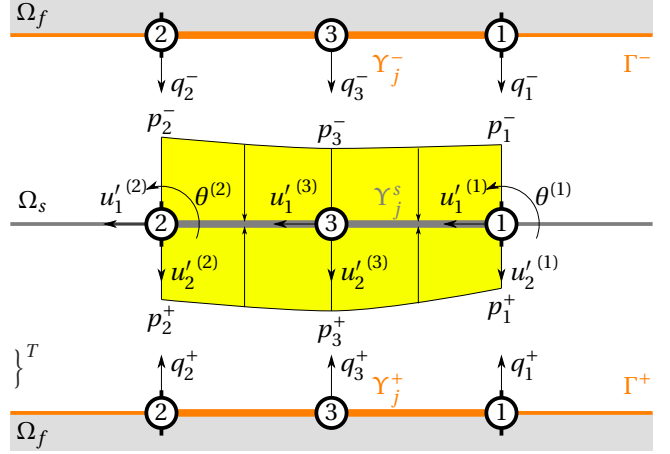

Figure 5: Coupling between sub-elements Υ_j^+, Υ_j^- and Υ_j^s (local numbering)

which are the compatibility equations for a node i. Note that these equations relate a primary variable of the structure (u) with a secondary variable of the fluid (pressure flux q). Thus, if the node i is a vertex node shared by two non-collinear elements, then the pressure flux q is undefined there (corner problem), being defined only just before and after the vertex. If both elements are almost collinear, and we are not interested in local effects, then it is acceptable assuming that the pressure flux is continuous. For this case, (29) is posed for each element and added up to build a unique compatibility condition. If both elements are far from collinear, the BEM variables of the vertex node are doubled, so that two sets of compatibility equations like (29) are posed. The pressure difference between both faces is equal to the lateral distributed load at each node of the beam:

$$s_2'^{(i)} = p_i^- - p_i^+ \qquad (30)$$

which is the equilibrium equation for a node i.

For each vertex node there are eight variables: p_i^+, q_i^+, p_i^-, q_i^-, $u_1^{(i)}$, $u_2^{(i)}$, $\theta^{(i)}$ and $s_2'^{(i)}$; and eight equations: SBIE for node i (15), HBIE for node i (16), 2 compatibility equations (29), 1 equilibrium (30), and 3 FEM equations from (27). For each central node, the situation is similar to the vertex node, except that the rotation and its associated FEM equation does not exist. Although the number of unknowns are equal to the number of equations, more conditions are required. The structure needs the necessary kinematic boundary conditions in order to avoid any rigid body motion.

The number of unknowns and equations for each node can be easily reduced from 8 to 6 (7 to 5 for the central node). It can be done by substituting (30) in (27), by using only the first equation of (29), and by substituting $q^+ = -q^-$ in (15) and (16) for every node of a BEM-FEM element. This reduction considerably decreases the computational effort.
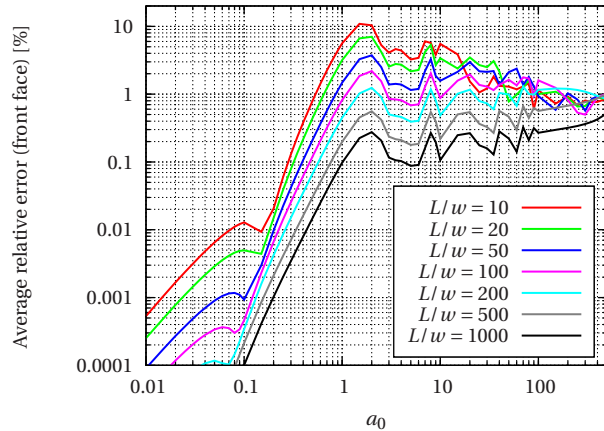
Figure 6: Average relative error of the null thickness assumption

Figure 7: Relative error of the null thickness assumption ($L/w = 100$)

2.4 Limitations

There are two relevant limitations in the proposed model: the null thickness assumption of the thin elastic body from the fluid point of view, and the Euler-Bernoulli hypotheses of the thin elastic body. For practical reasons, it is necessary establishing a validity range. Since studying the limitations using the complete FSI model needs many parameters, it seems to be more efficient studying each limitation in an uncoupled way.

The null thickness assumption can be studied considering the thin body as a rigid obstacle. Lacerda et al. [30] worked about this problem in the sound barriers field. They made a study comparing results from real geometries and their null thickness geometries at certain points and frequencies. It is interesting to expand and generalize this topic by using a dimensionless problem.

The experiment consists of a rectangular obstacle of length L and thickness w within a fluid $(\tilde{\rho}, \tilde{c})$, where a plane wave is propagating perpendicularly to the length with an angular frequency ω. The dimensionless frequency $a_0 = (\omega L)/\tilde{c}$ is used. Eight cases are solved: seven different geometrical slendernesses $L/w = \{10, 20, 50, 100, 200, 500, 1000\}$, and the case with null thickness. A conservative discretization of six quadratic elements per wavelength is used.

Figure 6 shows the average relative error of the pressure field over the front face of the obstacle versus the dimensionless frequency. It can be seen that the error decreases as geometrical slenderness increases, which is an obvious result. For $a_0 < 2$, the error decreases as a_0 decreases, being possible to define a frequency limit which ensures an error level. The maximum average error occurs around $a_0 = 2$, being: 10% for $L/w = 10$, 2% for $L/w = 100$ and 0.3% for $L/w = 1000$. For $a_0 > 2$, the error slowly increases if $L/w > 200$, and slowly decreases if $L/w < 200$.

Figure 7 shows the relative error of the pressure at some selected nodes of the front face versus the dimensionless frequency, for $L/w = 100$. For $a_0 < 1$ the error is approximate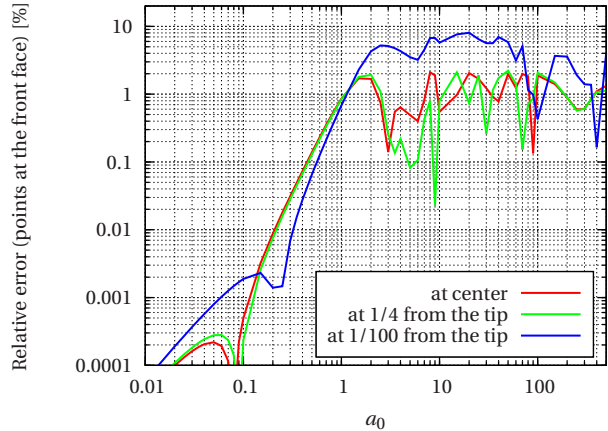ly the same at all points. For $a_0 > 1$, the error near the tip is around twice the error at points far from the tip. This behaviour also occurs for other slendernesses.

The Euler-Bernoulli hypotheses can be studied ignoring the fluid. A remarkable paper by Han et al. [22] studies the most widespread beam theories in dynamics, including our Euler-Bernoulli with added rotational inertia (called Rayleigh theory in that paper). Based on the study, Han et al. recommend using the Euler-Bernoulli theory when $L/w > 29$. Nevertheless, from [22, Figure 22], where the first natural frequency versus the mechanical slenderness is studied, it can be seen that the Euler-Bernoulli theory is appropriate even when $L/w > 10$.

Thus, the studied limitations have compatible validity ranges. The methodology is valid for geometrical slendernesses greater than 10. However, it must be taken into account that the error produced by the approximations depends on the dimensionless frequency and geometrical slenderness.

3 Results and discussion

3.1 Validation

The proposed model has been validated with results published by Jean [25], where a simple noise barrier problem is studied. The problem description is outlined in Figure 8. The fluid Ω_f is air with $\tilde{\rho} = 1.3 \, \text{kg/m}^3$ and $\tilde{c} = 340 \, \text{m/s}$. The thin elastic body Ω_s is a simple noise barrier 3 m high and 0.01 m thick, and it is clamped to the ground. Three different materials are considered for the barrier Ω_f (see Table 1). The ground is a perfectly reflecting surface, i.e. the fluid displacement at the ground is null. A point source located at $\mathbf{x}_s = (-2.3, 0.5)$ is used. The point source is easily added to the BEM equations, as shown in [37].

A comparison between results from Jean [25] and results from the proposed model is shown in Figure 9. The results from [25] are shown as a coloured background image from the original paper. The figure shows three graphs, one for each material. The y axis of each plot is the difference between pressures absolute values at a point $\mathbf{x}$ when using a rigid barrier
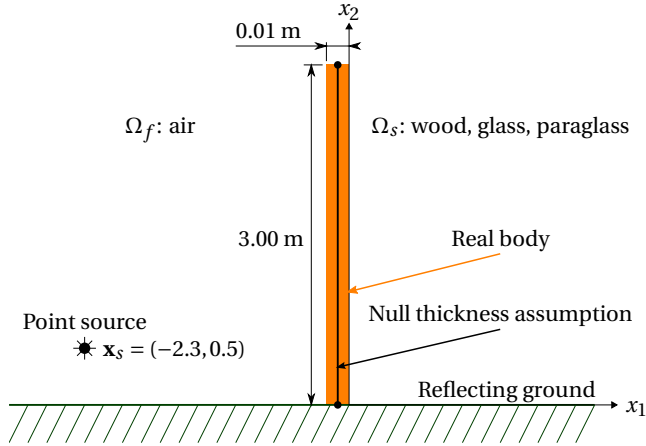
Figure 8: Noise barrier problem studied by Jean [25] (thickness not to scale)

Ω_s	$\rho\ \left[\text{kg/m}^3\right]$	$E\ \left[\text{MN/m}^2\right]$	ν	ξ
Wood	650	12.0	0.01	0.0100
Glass	2400	87.0	0.24	0.0005
Paraglass	1190	3.3	0.40	0.0150

Table 1: Materials for the barrier considered by Jean [25]

Figure 10: Layout for studying complex sound barrier shapes

Figure 11: *SIL* for different barrier shapes and materials

($q = 0$) and when using a flexible barrier. The natural frequencies f_n of each case are plotted as vertical lines, and they are calculated using the cantilever beam equations [14].

The model used in [25] takes into account the real geometry of the barrier, while the proposed model uses a null thickness barrier. The slenderness is $L/w = 333$, so from the barrier behaviour point of view, the Euler-Bernoulli hypotheses are valid. From the fluid behaviour point of view, the null thickness assumption is also valid, see section 2.4. Thus, the proposed model should be able to reproduce the results from [25].

Figure 9 shows excellent agreement between Jean's model and the proposed model. Peak frequencies and amplitudes are very well reproduced, although some small discrepancies appear in the wood case at frequencies around 850 Hz.

3.2 Complex sound barrier shapes

Jean [25] made a broad study comparing results between flexible and rigid simple sound barriers when varying material, thickness, damping coefficient, receiver and source position, and barrier height. In this section, the proposed model is used to study some complex barrier shapes.

The layout of the numerical experiments is depicted in Figure 10. Two simple screen barriers (simple barrier and double simple barrier) together with three multi-edge barrier shapes (Y barrier, U barrier and E barrier) are considered. For each shape, all materials from the Table 1 are used, the thickness is $w = 0.01$ m for all pieces, and the effective height is 3 m. The point source is located at ground level and 10 m ahead the barrier [46, 24, 37]. A grid of 3×11 receivers covering $6 \times 60\ \text{m}^2$ is
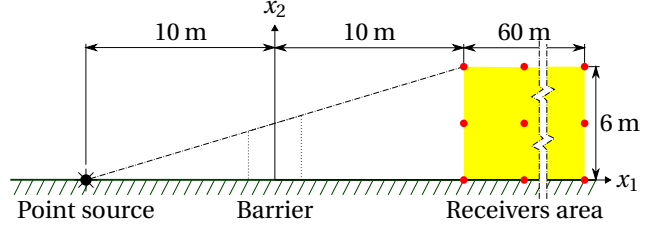
considered. A thousand frequencies uniformly distributed in $\log_{10}(f)$ space from $f_{\min} = 20$ Hz to $f_{\max} = 4000$ Hz are used.

Instead of taking the pressure as the variable of interest, the Insertion Loss *IL* is used [37]. The *IL* is the difference between pressures (in dB) when there is no barrier and when the barrier is placed, so it measures the efficiency of the barrier. We also consider the average Spectral Insertion Loss *SIL*, which is simply the average *IL* in the spectrum, leading to a frequency-independent indicator. The *IL* and the *SIL* are averaged values over all receivers.

In the literature, it is often assumed that noise barriers are rigid, so it is interesting finding when this hypothesis is valid or not. A first step is using the *SIL*, Figure 11 shows the *SIL* for all considered barrier shapes and materials, including the rigid case. It is seen that the rigid case is not conservative when using the *SIL* as an indicator. However, the maximum difference between the rigid case and any case is below 2 dB, being 1 dB for the simple barrier and double simple barrier, and 2 dB for the Y barrier. Thus, when a global indicator such as the *SIL* is going to be studied, the rigid assumption seems to be valid.

As Jean [25] showed for the simple barrier, when considering the elastic nature of the barrier there is a widespread pressure increment at low frequencies. Although this behaviour seems reasonable, it is interesting to analyse what happens when barriers more complex than the simple one are used. Figure 12 shows the *IL* spectrum for all studied barrier shapes and materials, including the rigid case.

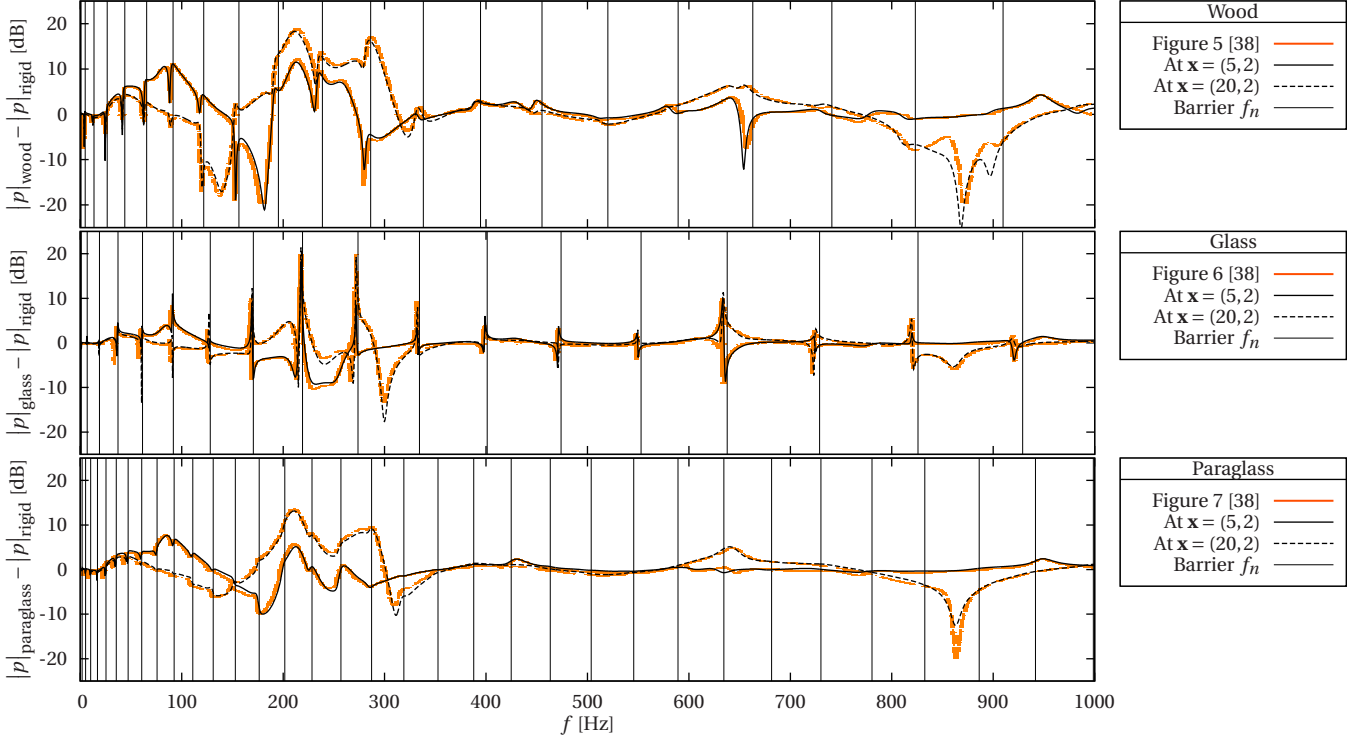For low frequencies ($f < 200\,\text{Hz}$) appreciable differences be-

Figure 9: Comparison between results from Jean [25] and results from the proposed model

tween rigid and flexible barriers are obtained. The simple barrier behaves as Jean described, with increments of pressure below 5 dB, i.e. *IL* decrements below 5 dB. The other barrier shapes have *IL* decrements below 10 dB. For very low frequencies ($f < 80$ Hz) there is virtually no noise attenuation. The considered complex barrier shapes strongly influence the *IL* spectrum, especially at low frequencies.

For mid-high frequencies ($f > 500$ Hz) the *IL* spectrum is very similar to a rigid barrier. For simple and double simple barriers, the differences are very small. For Y, U and E barriers, the differences are more noticeable, reaching up to 5 dB at some frequencies. Nevertheless, these differences seem to be irrelevant for noise propagation problems.

The human ear is less sensitive at low frequencies than at high frequencies, so, at first, this behaviour at low frequencies could be neglected. However, high frequencies are attenuated by losses in the air and on the absorbing surfaces, while low frequencies are not. Furthermore, when a building with windows closed is near the noise barrier, low frequency noises may be amplified inside the building. Therefore, depending on the context, the elasticity of a barrier similar to those studied should be considered.

3.3 Parametric study about a straight wall

In order to provide results of practical usage from this BEM-FEM approach, a simple but useful problem is studied. The problem consists of a straight wall (beam) ($2L, w, \rho, E_m, \nu, \xi$) with its centre clamped, surrounded by a fluid ($\tilde{\rho}, \tilde{c}$), where a pressure plane wave is propagating with unity amplitude, perpendicular direction, and angular frequency ω, see Figure 13.

The problem parameters can be reduced to six dimensionless ones:

- Wave propagation speeds ratio: $\tilde{c}/c$, where $c = \sqrt{E_m/\rho}$ is the beam axial wave propagation speed.

- Densities ratio: $\tilde{\rho}/\rho$.

- Geometrical slenderness: L/w.

- Dimensionless frequency: $a_0 = (\omega L)/\tilde{c}$.

- Damping coefficient: ξ

- Poisson's ratio: ν

Table 2 shows the studied values of the dimensionless parameters. The wave propagation speeds ratio and the densities ratio have ranges that include the most extreme fluid-structure combinations. The geometrical slenderness starts from $L/w = 10$ to $L/w = 1000$, which are within the validity interval. The dimensionless frequency range has been chosen so that at least the first natural frequency is clearly captured in all cases.

This parametric study is oriented to know the FSI coupling degree. It seems obvious that a decoupled model could be used for extreme cases, e.g. a thick steel wall in air. In these extreme cases, the pressure field in the air is calculated considering a rigid obstacle, and if needed, the pressure field can be
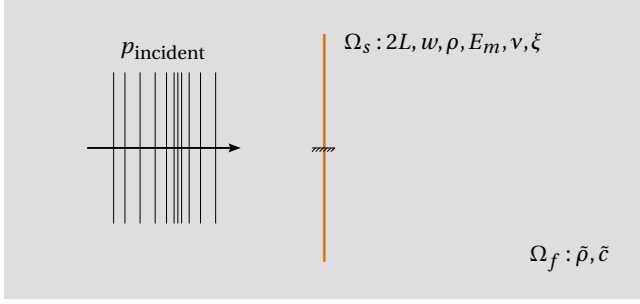
9

Figure 13: Problem configuration

Parameter	Studied values
ξ	0.05
ν	0.30
$\tilde{c}/c$	$\{1/50, 1/20, 1/10, 1/5, 1/2, 1/1, 2/1\}$
$\tilde{\rho}/\rho$	$\{1/10^5, 1/10^4, 1/10^3, 1/10^2, 1/10, 1/1, 10/1\}$
L/w	$\{10, 20, 50, 100, 200, 500, 1000\}$
a_0	$[10^{-4}, 10]$

Table 2: Studied values of each dimensionless parameter

Figure 14: Average relative pressure differences with respect to the rigid case ($\tilde{c}/c = 1/5$)

Figure 15: First natural frequencies $\tilde{\omega}_1/\omega_1$ ratio ($\tilde{c}/c = 1/5$)

used as the obstacle load. However, there are cases like a thin wall in water, or a thin steel wall in oil, etcetera, where interaction relevance is not so clear. All dimensionless parameters combinations of Table 2 are studied.

Figure 14 shows the average relative pressure difference at nodes between a given case and the rigid case. The relative pressure difference is averaged over frequencies. It has been built in order to know if a wall could be considered rigid or not when one is interested in the pressure field. It has been found that the wave propagation speeds ratio has a small influence over it, so only $\tilde{c}/c = 1/5$ is used in the figure. The densities ratio and the geometrical slenderness strongly influence the average relative pressure differences. The contour lines clearly show that, for a given pressure difference, there is a region where the straight beam can be considered rigid. A rule of thumb can be established: for $L/w < 1000$, if $\tilde{\rho}/\rho < 1/1000$, the straight beam can be considered rigid.

Figure 15 shows the $\tilde{\omega}_1/\omega_1$ ratio, where $\tilde{\omega}_1$ is the first natural frequency of the fluid-structure system, and ω_1 is the first natural frequency of the structure in vacuum [14]. It has been built in order to know if the fluid must be taken into account when one is interested in the straight beam behaviour. Analogously to the previous analysis, the wave propagation speeds ratio has a small influence over $\tilde{\omega}_1/\omega_1$, so $\tilde{c}/c = 1/5$ is used in the figure. The densities ratio and the geometrical slenderness are the main influences over the variable of interest. The $\tilde{\omega}_1/\omega_1$ ratio is < 1, so the fluids roughly acts as an added mass. The obtained $\tilde{\omega}_1/\omega_1$ contour lines can be used to quantify the fluid influence over the FSI problem.
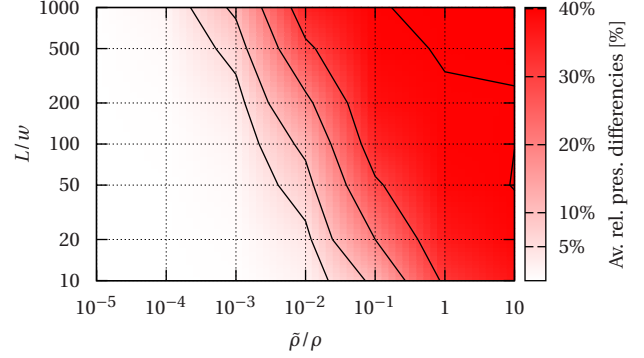
4 Conclusions

In this paper, a 2D BEM-FEM approach for dynamic fluid-structure problems when structures have small thicknesses is presented. The fluid is considered homogeneous, inviscid, at rest, without body forces, and with linear behaviour. From the fluid point of view, the structure is seen as a null thickness body. The null thickness assumption is treated using the SBIE/HBIE dual formulation for thin bodies, which is developed in detail, showing that only regular and weakly singular integrals remain. A quadratic BE for pressure and pressure flux interpolation is used. The structure is under the Euler-Bernoulli hypotheses with added rotational inertia, which is discretized using the FEM. An eight degrees of freedom FE which incorporates displacements and rotations is used. The BEM and the FEM equations are coupled using appropriate equilibrium and compatibility conditions, which allows defining a BEM-FEM fluid-structure element for thin structures.

This approach has been validated with existing results of

sound diffraction around a simple straight noise barrier [25]. For this problem, the vibro-acoustical response has remarkable differences when compared with the response using the rigid hypothesis. It also varies considerably with the chosen material. The obtained results show excellent agreement.

The potential of this methodology is shown through two problems. The first problem is the study of some complex multi-edge barrier shapes using the same materials as the validation problem. The effects of considering the elasticity of the barrier are more noticeable for these complex barrier shapes than for the simple barrier. Thereby, at low frequencies ($f <$ 200 Hz) flexible barriers are less efficient, especially at very low frequencies ($f <$ 80 Hz), where there is virtually no noise attenuation. At mid-high frequencies ($f >$ 500 Hz), the differences between rigid cases and flexible cases are small. However, these differences are visible in the whole range of studied frequencies, being stronger with the Y, U, and E barrier shapes. The second problem is a parametric study over a straight wall surrounded by a fluid where a perpendicularly incident plane wave is propagating. The coupling degree from the fluid and the structure points of view is shown.

A M_2 regularization process

The key point of the regularization is using $\partial r / \partial \Gamma = (\mathbf{r}/r) \cdot \mathbf{t}$, where $\mathbf{t}$ is the unit tangent of the boundary Γ. $\partial r / \partial \Gamma$ has a jump discontinuity from -1 to 1 at the collocation point (see Figure 16). If $|\partial r / \partial \Gamma|$ is considered, then a Taylor expansion for $r \to 0$ can be done:

$$\left| \frac{\partial r}{\partial \Gamma} \right| = \cos \alpha = 1 + \mathcal{O}\left(\alpha^2\right) = 1 + \mathcal{O}\left(r^2\right) \tag{31}$$

where $\alpha \propto r$ when $r \to 0$. The dot product $(\mathbf{n}_i \cdot \mathbf{n})$ behaves in the same way as $|\partial r / \partial \Gamma|$ does when $r \to 0$ (see Figure 16):

$$(\mathbf{n}_i \cdot \mathbf{n}) = \cos \alpha = 1 + \mathcal{O}\left(\alpha^2\right) = 1 + \mathcal{O}\left(r^2\right) \tag{32}$$

In M_2, if $|\partial r / \partial \Gamma|$ is added up and substracted from $\mathbf{n}_i \cdot \mathbf{n}$:

$$M_2 = \frac{1}{2\pi} \lim_{\epsilon \to 0} \int_{\Gamma - e_i^\epsilon} \frac{1}{r^2} \left[(\mathbf{n}_i \cdot \mathbf{n}) - \left| \frac{\partial r}{\partial \Gamma} \right| \right] p \, d\Gamma + \frac{1}{2\pi} \lim_{\epsilon \to 0} \int_{\Gamma - e_i^\epsilon} \frac{1}{r^2} \left| \frac{\partial r}{\partial \Gamma} \right| p \, d\Gamma =$$
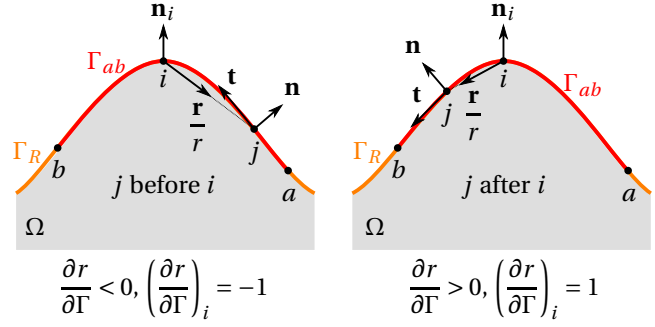
$$= M_{21} + M_{22} \tag{33}$$

Figure 16: Behaviour of several vectors near the collocation point

where M_{21} is regular, but M_{22} is hypersingular. Because $p\left(\mathbf{x}_i\right) \in \mathscr{C}^1$, one can write a Taylor expansion of p around the collocation point:

$$p = p_i + \left(\frac{\partial p}{\partial r} \right)_i r + \mathcal{O}\left(r^2\right) \tag{34}$$

where $(\partial p / \partial r)_i = (\partial p / \partial \Gamma)_i / (\partial r / \partial \Gamma)_i$, and $\left(\partial p / \partial \Gamma \right)_i$ is the pressure tangential derivative at the collocation point. In M_{22}, if $p_i + (\partial p / \partial r)_i r$ is added up and substracted from p:

$$M_{22} = \frac{1}{2\pi} \lim_{\epsilon \to 0} \int_{\Gamma - e_i^\epsilon} \frac{1}{r^2} \left| \frac{\partial r}{\partial \Gamma} \right| \left[p - p_i - \left(\frac{\partial p}{\partial r} \right)_i r \right] d\Gamma +$$

$$+ \frac{1}{2\pi} p_i \lim_{\epsilon \to 0} \int_{\Gamma - e_i^\epsilon} \frac{1}{r^2} \left| \frac{\partial r}{\partial \Gamma} \right| d\Gamma + \frac{1}{2\pi} \lim_{\epsilon \to 0} \int_{\Gamma - e_i^\epsilon} \frac{1}{r} \left| \frac{\partial r}{\partial \Gamma} \right| \left(\frac{\partial p}{\partial r} \right)_i d\Gamma =$$

$$= M_{221} + M_{222} + M_{223} \tag{35}$$

where M_{221} is regular, M_{222} is hypersingular, and M_{223} is strongly singular. In order to treat M_{222}, Γ is split in two parts: Γ_R and Γ_{ab}. Γ_{ab} is a portion of Γ that contains the collocation point, and Γ_R is the complementary portion, which is regular. Given any collocation point $i \in \Gamma_{ab}$ and any other observation point $j \in \Gamma_{ab}$, the portion Γ_{ab} must meet also that: if j is before i then $\partial r / \partial \Gamma < 0$, and if j is after i then $\partial r / \partial \Gamma > 0$. A regular part and a singular part is obtained from M_{222}:

$$M_{222} = \frac{1}{2\pi} p_i \int_{\Gamma_R} \frac{1}{r^2} \left| \frac{\partial r}{\partial \Gamma} \right| d\Gamma + \frac{1}{2\pi} p_i \lim_{\epsilon \to 0} \int_{\Gamma_{ab} - e_i^\epsilon} \frac{1}{r^2} \frac{\left| \frac{\partial r}{\partial \Gamma} \right|}{\frac{\partial r}{\partial \Gamma}} \, dr =$$

$$= M_{222})_R + M_{222})_{ab} \tag{36}$$

From the singular part, an unbounded term that cancels out the one that appears in (8) emerges together with a finite part:

$$M_{222})_{ab} = \frac{1}{2\pi} p_i \left[\lim_{\epsilon \to 0} \int_{|\mathbf{r}_b|}^\epsilon \frac{(-1)}{r^2} \, dr + \lim_{\epsilon \to 0} \int_\epsilon^{|\mathbf{r}_a|} \frac{(+1)}{r^2} \, dr \right] =$$

$$= \frac{p_i}{\pi} \lim_{\epsilon \to 0} \left(\frac{1}{\epsilon} \right) - \frac{p_i}{2\pi} \left(\frac{1}{|\mathbf{r}_a|} + \frac{1}{|\mathbf{r}_b|} \right)$$

11

$$ \tag{37} $$

where $\mathbf{r}_b$ and $\mathbf{r}_a$ are distance vectors of the extreme points of Γ_{ab}. The integral M_{223} is treated similarly to M_{222}:

$$ M_{223} = \frac{1}{2\pi}\left(\frac{\partial p}{\partial \Gamma}\right)_i \int_{\Gamma_R} \frac{1}{r}\frac{\left|\frac{\partial r}{\partial \Gamma}\right|}{\left(\frac{\partial r}{\partial \Gamma}\right)_i}\, \mathrm{d}\Gamma + \frac{1}{2\pi}\left(\frac{\partial p}{\partial \Gamma}\right)_i \lim_{\epsilon \to 0} \int_{\Gamma_{ab} - e_i^\epsilon} \frac{1}{r}\frac{\left|\frac{\partial r}{\partial \Gamma}\right|}{\frac{\partial r}{\partial \Gamma}\left(\frac{\partial r}{\partial \Gamma}\right)_i}\, \mathrm{d}r $$

$$ = M_{223})_R + M_{223})_{ab} \tag{38} $$

It is easy to see that $\partial r/\partial \Gamma\,(\partial r/\partial \Gamma)_i = |\partial r/\partial \Gamma|$ in $\Gamma_{ab}-e_i^\epsilon$. Therefore, $M_{223})_{ab}$ is analytically solvable:

$$ M_{223})_{ab} = \frac{1}{2\pi}\left(\frac{\partial p}{\partial \Gamma}\right)_i \lim_{\epsilon \to 0} \int_{\Gamma_{ab} - e_i^\epsilon} \frac{1}{r}\, \mathrm{d}r = \frac{1}{2\pi}\left(\frac{\partial p}{\partial \Gamma}\right)_i \left(\ln|\mathbf{r}_b| - \ln|\mathbf{r}_a|\right) \tag{39} $$

Once the regularized M_2 is introduced in (8), the regularized HBIE is obtained:

$$ \frac{1}{2}\left(\frac{\partial p}{\partial n_i}\right)_i + M_1 + M_{21} + M_{221} + $$
$$ + M_{222})_R - \frac{p_i}{2\pi}\left(\frac{1}{|\mathbf{r}_a|} + \frac{1}{|\mathbf{r}_b|}\right) + M_{223} + M_3 = L \tag{40} $$

References

[1] M. Abramowitz and I.A. Stegun. *Handbook of Mathematical Functions: with Formulas, Graphs, and Mathematical Tables.* Number 55 in Applied Mathematics. New York, Dover Publications, 1964.

[2] M.P. Ariza and J. Domínguez. General BE approach for three-dimensional dynamic fracture analysis. *Engineering Analysis with Boundary Elements*, 26:639–651, 2002.

[3] J.J. Aznárez, O. Maeso, and J. Domínguez. BE analysis of bottom sediments in dynamic fluid-structure interaction problems. *Engineering Analysis with Boundary Elements*, 30:124–136, 2006.

[4] A.A. Becker. *The Boundary Element Method in Engineering.* McGraw-Hill International, 1992.

[5] D.E. Beskos. Boundary Element Methods in Dynamic Analysis. *Applied Mechanics Reviews*, 40(1):1–23, 1987.

[6] D.E. Beskos. Boundary Element Methods in Dynamic Analysis: Part II (1986-1996). *Applied Mechanics Reviews*, 50(3):149–197, 1997.

[7] G.E. Blandford, A.R. Ingraffea, and J.A. Liggett. Two-dimensional stress intensity factor computations using the boundary element method. *International Journal for Numerical Methods in Engineering*, 17(3):387–404, 1981.

[8] C.A. Brebbia and R.D. Ciskowski, editors. *Boundary Element Methods in Acoustics.* Springer, 1991.

[9] C.V. Camp and G.S. Gipson. Overhauser elements in boundary element analysis. *Mathematical and Computer Modelling*, 15:56–69, 1991.

[10] J.T. Chen and H.-K. Hong. Review of dual boundary element methods with emphasis on hypersingular integrals and divergent series. *Applied Mechanics Review*, 52(1):17–33, 1999.

[11] L.L. Chen, H.B. Chen, and C.J. Zheng. FEM/Wideband FMBEM coupling for fluid-structure interaction problem and 2D acoustic design sensitivity analysis. *Computer Modeling in Engineering and Sciences*, 94(6):459–483, 2013.

[12] S. Chen and Y. Liu. A unified boundary element method for the analysis of sound and shell-like structure interactions. I. Formulation and verification. *Journal of Acoustical Society of America*, 106(3):1247–1254, 1999.

[13] Z.S. Chen, G. Hofstetter, and H.A. Mang. A symmetric galerkin formulation of the Boundary Element Method for acoustic radiation and scattering. *Journal of Computational Acoustics*, 5(2):219–241, 1997.

[14] R.W. Clough and J. Penzien. *Dynamics of Structures.* Computers and Structures, Incorporated, 2003.

[15] T.A. Cruse. Two-dimensional BIE fracture mechanics analysis. *Applied Mathematical Modelling*, 2:287–293, 1978.

[16] J. Domínguez. *Boundary Elements in Dynamics.* International Series on Computational Engineering. Computational Mechanics Publications, 1993.

[17] J. Domínguez, M.P. Ariza, and R. Gallego. Flux and traction boundary elements without hypersingular or strongly singular integrals. *International Journal for Numerical Methods in Engineering*, 48:111–135, 2000.

[18] R. Gallego and J. Domínguez. Hypersingular BEM for transient elastodynamics. *International Journal for Numerical Methods in Engineering*, 39:1681–1705, 1996.

[19] L.J. Gray. Evaluation of hypersingular integrals in the boundary element method. *Mathematical and Computer Modelling*, 15:165–174, 1991.

[20] M. Guiggiani, G. Krishnasamy, T.J. Rudolphi, and F.J. Rizzo. A general algorithm for the numerical solution of hypersingular boundary integral equations. *Journal of Applied Mechanics*, 59:604–614, 1992.

[21] W.S. Hall and G. Oliveto, editors. *Boundary Element Methods for Soil-Structure Interaction.* Kluwer Academic Publishers, 2004.

[22] S.M. Han, H. Benaroya, and T. Wei. Dynamics of transversely vibrating beams using four engineering theories. *Journal of Sound and Vibration*, 225(5):935–988, 1999.

[23] H.-K Hong and J.T. Chen. Derivations of integral equations of elasticity. *Journal of Engineering Mechanics*, 114(6):1028âĂŞ1044, 1988.

[24] D.C. Hothersall, D.H. Crombie, and S.N. Chandler-Wilde. Efficiency of single noise barriers. *Journal of Sound and Vibration*, 146(2):303–322, 1991.

[25] P. Jean. The effect of structural elasticity on the efficiency of noise barriers. *Journal of Sound and Vibration*, 237(1):1–21, 2000.

[26] L. Jun, G. Beer, and J.L. Meek. Efficient evaluation of integrals of order $1/r$, $1/r^2$ and $1/r^3$ using Gauss quadrature. *Engineering Analysis*, 2(3):118–123, 1985.

[27] G. Krishnasamy, F.J. Rizzo, and Y. Liu. Boundary integral equations for thin bodies. *International Journal for Numerical Methods in Engineering*, 37:107–121, 1994.

[28] G. Krishnasamy, F.J. Rizzo, and T.J. Rudolphi. Hypersingular boundary integral equations: Their occurrence, interpretation, regularization and computation. In P.K. Banerjee and S. Kobayashi, editors, *Developments in Boundary Element Methods*. Elsevier Applied Science, 1991.

[29] G. Krishnasamy, F.J. Rizzo, and T.J. Rudolphi. Continuity requirements for density functions in the boundary integral equation method. *Computational Mechanics*, 9:267–284, 1992.

[30] L.A. Lacerda, L.C. Wrobel, and W.J. Mansur. A dual boundary element formulation for sound propagation around barriers over an impedance plane. *Journal of Sound and Vibration*, 202(2):235–247, 1997.

[31] L.A. Lacerda, L.C. Wrobel, H. Power, and W.J. Mansur. A novel boundary integral formulation for three-dimensional analysis of thin acoustic barriers over an impedance plane. *Journal of Acoustical Society of America*, 104(2):671–678, 1998.

[32] J.C. Lachat and J.O. Watson. Effective numerical treatment of boundary integral equations: a formulation for three-dimensional elastostatics. *International Journal for Numerical Methods in Engineering*, 10:991–1005, 1976.

[33] J.A. Liggett and J.R. Salmon. Cubic spline boundary elements. *International Journal for Numerical Methods in Engineering*, 17(4):543–556, 1981.

[34] Y. Liu. Analysis of shell-like structures by the boundary element method based on 3-D elasticity: formulation and verification. *International Journal for Numerical Methods in Engineering*, 41:541–558, 1998.

[35] Y. Liu, D. Zhang, and F.J. Rizzo. Nearly singular and hypersingular integrals in the boundary element method. In *Proceedings of the 15th International Conference on Boundary Elements*, pages 453–468, Worcester, Massachusetts, USA, August 1993.

[36] J.F. Luo, Y. Liu, and E.J. Berger. Analysis of two-dimensional thin structures (from micro- to nano- scales) using the boundary element method. *Computational Mechanics*, 22:404–412, 1998.

[37] O. Maeso and J.J. Aznárez. *Estrategias para la reducción del impacto acústico en el entorno de carreteras. Una aplicación del método de los elementos de contorno*. Universidad de Las Palmas de Gran Canaria, 2005. in Spanish.

[38] S. Marburg. *Computational Acoustics of Noise Propagation in Fluids - Finite and Boundary Element Methods*, chapter 11. Discretization Requirements: How many Elements per Wavelength are Necessary?, pages 309–332. Springer, 2008.

[39] P.A. Martin and F.J. Rizzo. Hypersingular integrals: how smooth must the density be? *International Journal for Numerical Methods in Engineering*, 39:687–704, 1996.

[40] P.A. Martin, F.J. Rizzo, and T.A. Cruse. Smoothness-relaxation strategies for singular and hypersingular integral equations. *International Journal for Numerical Methods in Engineering*, 42:885–906, 1998.

[41] F. Medina, J. Domínguez, and J. Tassoulas. Response of dams to earthquakes including effects of sediments. *Journal of Structural Engineering*, 116(11):3108–3121, 1990.

[42] L.A. Padrón, J.J. Aznárez, and O. Maeso. BEM-FEM coupling model for the dynamic analysis of piles and pile groups. *Engineering Analysis with Boundary Elements*, 31:473–484, 2007.

[43] L.A. Padrón, J.J. Aznárez, and O. Maeso. Dynamic analysis of piled foundations in stratified soils by a BEM-FEM model. *Soil Dynamics and Earthquake Engineering*, 28:333–346, 2008.

[44] L.A. Padrón, J.J. Aznárez, O. Maeso, and A. Santana. Dynamic stiffness of deep foundations with inclined piles. *Earthquake Engineering and Structural Dynamics*, 39:1343–1367, 2010.

[45] A. Sáez, R. Gallego, and J. Domínguez. Hypersingular quarter-point boundary elements for crack problems. *International Journal for Numerical Methods in Engineering*, 38:1681–1701, 1995.

[46] R. Seznec. Diffraction of sound around a barrier: use of the boundary elements technique. *Journal of Sound and Vibration*, 73:195–209, 1980.

[47] V. Sladek and J. Sladek. Three dimensional crack analysis for an anisotropic body. *Applied*, 6:374–380, 1982.

[48] A. Tadeu, J. António, P. Amado, and L. Godinho. Sound pressure level attenuation provided by thin rigid screens coupled to tall buildings. *Journal of Sound and Vibration*, 304:479–496, 2007.

[49] A. Tadeu, J. António, L. Godinho, and P. Amado. Simulation of sound absorption in 2d thin elements using a coupled BEM/TBEM. *Journal of Sound and Vibration*, 331:2386–2403, 2012.

[50] A. Tadeu and L. Godinho. Scattering of acoustic waves by movable lightweight elastic screens. *Engineering Analysis with Boundary Elements*, 27:215–226, 2003.

[51] M. Tanaka, V. Sladek, and J. Sladek. Regularization techniques applied toboundary element methods. *Applied Mechanics Reviews*, 47:457–499, 1994.

[52] J.C.F. Telles. A self-adaptive co-ordinate transformation for efficient numerical evaluation of general boundary element integrals. *International Journal for Numerical Methods in Engineering*, 24:959–973, 1987.

[53] J.C.F. Telles and R.F. Oliveira. Third degree polynomial transformation for boundary element integrals: further improvements. *Engineering Analysis with Boundary Elements*, 13:135–141, 1994.

[54] O. von Estorff, editor. *Boundary Elements in Acoustics.* WIT Press, 2000.

[55] G. Xie, F. Zhou, J. Zhang, X. Zheng, and C. Huang. New variable transformations for evaluating nearly singular integrals in 2D boundary element method. *Engineering Analysis with Boundary Elements*, 35:811–817, 2011.

[56] G. Xie, F. Zhou, J. Zhang, X. Zheng, and C. Huang. New variable transformations for evaluating nearly singular integrals in 3D boundary element method. *Engineering Analysis with Boundary Elements*, 37:1169–1178, 2013.

[57] Y. Zhang, Y. Gu, and J.T. Chen. Boundary element analysis of 2D thin walled structures with high-order geometry elements using transformation. *Engineering Analysis with Boundary Elements*, 35:581–586, 2011.
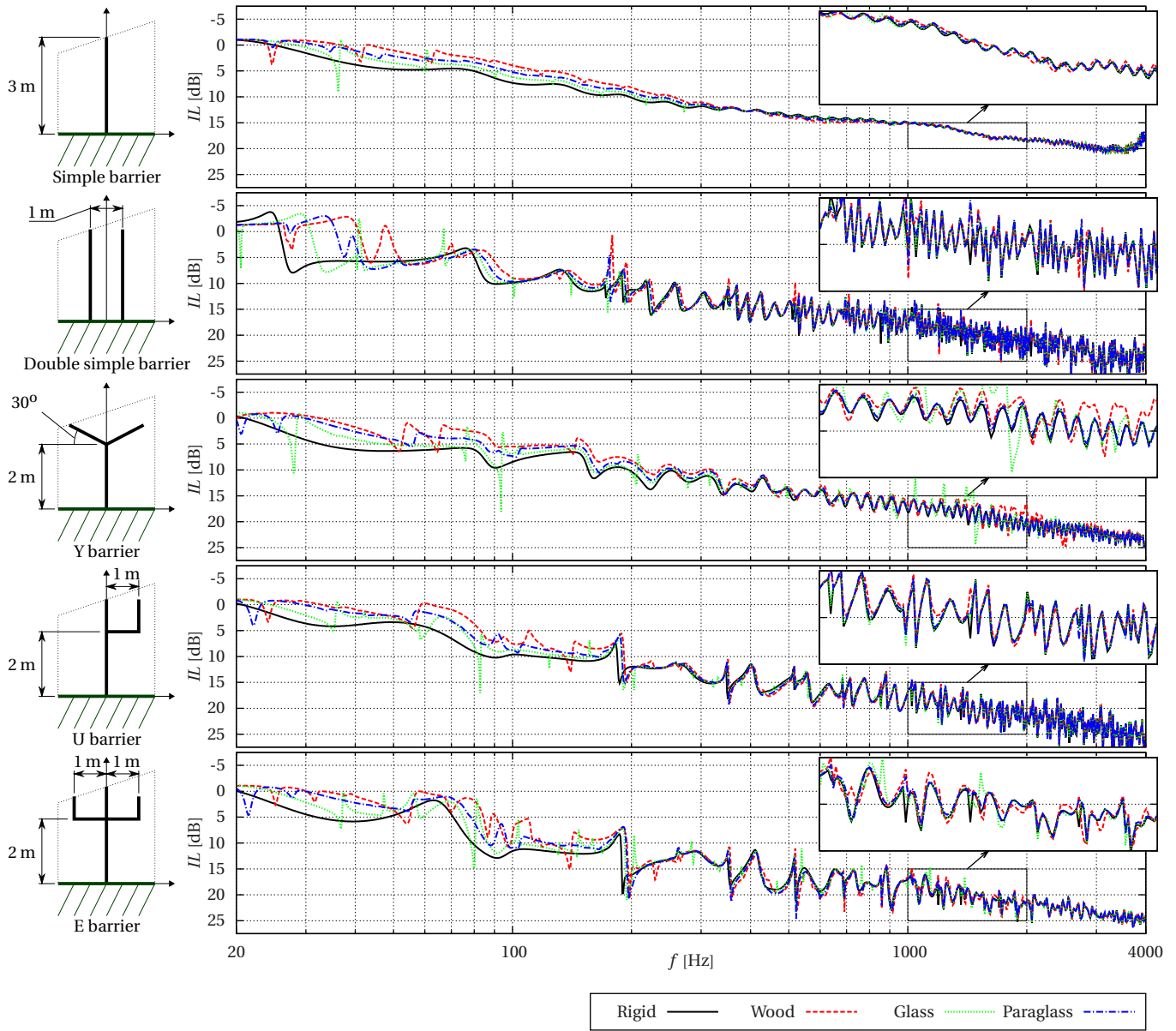
Figure 12: *IL* for different barrier shapes and materials